The role of the intermediate state in angle-resolved photoelectron studies using (2+1) resonance-enhanced multiphoton ionization of the chiral terpenes, α-pinene and 3-carene.

Hassan Ganjitabar [a],
Dhirendra P. Singh [a],
Richard Chapman [b]
Adrian Gardner [a,c],
Russell S. Minns [d],
Ivan Powis[a]*,
Katharine L. Reid [a],
Arno Vredenborg [e,f]

a) School of Chemistry, The University of Nottingham, University Park, Nottingham NG7 2RD, UK

b) Central Laser Facility, STFC Rutherford Appleton Laboratory, Didcot, Oxfordshire OX11 0QX, UK

c) Stephenson Institute for Renewable Energy and the Department of Chemistry, University of Liverpool, Liverpool, L69 7ZD, UK

d) School of Chemistry, University of Southampton, Highfield, Southampton SO17 1BJ,

e) Institute for Molecules and Materials, Radboud University Nijmegen, Heyendaalseweg 135, 6525 AJ Nijmegen, The Netherlands

f) MassSpecpecD BV, Langenkampweg 101, 7522 LL Enschede, The Netherlands

*Corresponding Author:
Tel: +44 115 9513467
E-mail: ivan.powis@nottingham.ac.uk

Paper Submitted for the Dave Parker Special issue

Abstract

Photoelectron angular distributions (PADs), ranging up to the maximum 6^{th} order Legendre polynomial term set by the Yang theorem, have been recorded for the (2+1) resonance enhanced multiphoton ionization (REMPI) of two terpene isomers, 3-carene and α-pinene, employing femtosecond lasers and electron velocity map imaging detection. PAD measurements made with coincident photoion detection allow ion fragmentation effects to be assessed. Using circular polarization and enantiomerically pure samples the PAD measurements are extended to include chiral (odd) Legendre polynomial terms, and these are analyzed and discussed as multiphoton photoelectron circular dichroism (MP-PECD). Comparisons are also made with single photon (synchrotron radiation) PECD of these compounds. Although for a given compound a common final cation state is reached, pronounced differences are observed between PECD and MP-PECD, and between the alternative identified REMPI intermediate states in the case of MP-PECD.

Introduction

Since its inception, the technique of Velocity Map Imaging (VMI) has been closely associated with pulsed laser experiments, where its efficient 4π acceptance and highly multiplexed energy and angular detection, readily compensates for any duty cycle limitations. VMI has undoubtedly also contributed to a resurgence of interest in studying photoelectron spectroscopy, and particularly photoelectron angular distribution measurements that extend beyond the traditional anisotropy parameter β. Here again, the sensitivity and multiplexing now allow angular distribution parameters to be extracted with precision, and when pulsed laser multiphoton excitation is employed measurements can be extended to weaker and higher harmonics of the distribution.

Photoelectron circular dichroism (PECD) experiments using circularly polarized synchrotron radiation to study chiral molecules have often used VMI detection [1]. PECD extracts an additional first Legendre polynomial term that describes a chiral forward-backward asymmetry in the photoelectron scattering and a substantial literature has grown around the significant insights into the static and dynamical structure that this provides [2]. More recently, there has been a developing interest in multiphoton excited PECD (MP-PECD), where additional chiral harmonics can be expected, and both fundamental investigations and analytical applications can be foreseen [3].

Despite its prevalence in pulsed laser excitation experiments, VMI has often made use of 2-dimensional (*x,y*) position sensitive detector systems that lack the time resolution to exploit direct time-of-flight measurements. Information from a 2-D detector image is then typically extracted using inverse-Abel mathematical transformations [4]. Alternative detector technologies can provide fast, sub nanosecond, timing resolution that can be used for a full 3-dimensional detection, obviating the need for Abel inversion (and with it the implied restriction to experimental geometries that maintain cylindrical symmetry). Fast timing also permits use in, for example, electron-ion coincidence imaging applications [5,6]. In the context of photoelectron studies, coincidence detection permits mass/size selected electron images to be recorded, capable of distinguishing photoionization of dimer and cluster species [7], or of components in a gaseous mixture [8].

The normalized photoelectron angular distribution obtained in multiphoton ionization with identical photons can be written [9] as

$$I^{\{p\}}(\theta) = 1 + \sum_{j=1}^{2n} b_j^{\{p\}} P_j(\cos\theta) \quad (1)$$

where the upper limit on the summation over Legendre polynomials, P_j , is fixed according to Yang's theorem [10] by *n*, the number of photons involved in the process. In fact, in his original paper Yang envisages only *even* harmonics in the summation of Eq. (1), but it is now recognized that *odd* harmonics arise when chiral molecules are ionized with circularly polarized light (CPL) [11]. With the light polarization index $p = \pm 1$ then indicating, respectively, left- and right- CPL, the angle θ is measured with respect to the light beam propagation direction. The odd Legendre polynomials in Eq. (1), expand to predict a forward-backward asymmetry in the photoelectron angular distribution, modulated in magnitude and direction by the associated of $b_j^{\{p=\pm 1\}}$ coefficients. Without both circular polarization and chiral molecular targets the odd harmonics necessarily vanish.

Unlike the even b_j coefficients which are symmetric, the odd coefficients are antisymmetric, changing sign with a switch between left- and right-handed CPL (or with exchange of enantiomer). Consequently, the subtraction $I^{\{+1\}}(\theta) - I^{\{-1\}}(\theta)$ leads to a cancellation of the even terms, and effectively isolates the odd terms. Proceeding via this difference image (dichroism) has the additional experimental advantage of cancelling out purely instrumental asymmetry contributions and is a justification for the PECD approach over simply attempting the determination of all angular parameters from a single polarization image.

For discussing MP-PECD measurements it is often convenient to define a Kuhn asymmetry factor [12] providing a single numerical measure of the chiral asymmetry of the photoelectron:

$$G_{AD} = \left(I_{fwd} - I_{back}\right) \Big/ \tfrac{1}{2}\left(I_{fwd} + I_{back}\right) \quad (2)$$

where I_{fwd} and I_{back} are, respectively, the integrated electron count emitted into the forward and backward facing hemispheres, relative to the light propagation direction. The asymmetry, G_{AD} , will, like the underlying photoionization dynamics, be dependent on the electron kinetic energy. It can be shown [13,14] that in terms of the angular distribution parameters

$$G_{AD}^{\{p\}} = 2b_1^{\{p\}} - \tfrac{1}{2} b_3^{\{p\}} + \tfrac{1}{4} b_5^{\{p\}} \ldots \quad (3)$$

Note that the sign of G_{AD} will depend on specifying the polarization state *p* (or the subtraction order in Eq. (2)), but also the enantiomer. Switching enantiomer will cause all the terms appearing in Eq. (3) to change sign. By convention we will always specify these asymmetries for *p* = +1.

While a wide range of chiral molecular systems have been investigated by single-photon PECD experiments utilizing synchrotron radiation [2], MP-PECD has to date been concerned with studies made with just a few test-case systems, notably camphor and fenchone [8,14-21], and to a lesser degree limonene [13,21,22] and methyl oxirane [23]. In this paper we describe MP-PECD measurements made using fs laser (2+1) REMPI ionization with two further chiral terpene molecules, 3-carene and α-pinene, Scheme 1. We use two VMI spectrometers equipped with a standard 2D detector arrangement and a 3D electron-ion coincidence imaging detector system to further help characterize our observations.

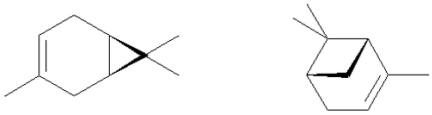

1S-(+)-3-carene 1S-(-)-α-pinene

Scheme 1

Experimental

The results presented in this work are the outcome of two separate femtosecond laser experiments; one at the Artemis beamline of the STFC Central Laser Facility (CLF) and the other at LaserLab Europe (Radboud University).

At the Artemis beamline, 50 fs pulses of 800 nm light, with a repetition rate of 1 kHz were generated by an amplified femtosecond laser system (Red Dragon, KM Labs). A BBO frequency doubling crystal was used to produce the 396 nm wavelength as the second harmonic of the fundamental wavelength while the 371 nm wavelength was generated using an optical parametric amplifier (OPA, TOPAS Light Conversion). At Radboud University, the fundamental output of a 150 fs Ti-sapphire laser system at 3 KHz repetition rate, was tuned and frequency doubled to produce either a 400 nm or 407 nm second harmonic. In either setup left or right circularly polarized light (LCP or RCP) was generated from the linearly polarized outputs using a quarter-wave plate, and the polarization checked using a second rotating quarter-waveplate polarimeter[24]. Detailed specifications of the laser light, as well as the results of the polarimetry, appear in Table 1.

REMPI electron imaging of 1S-(-)-α-pinene was recorded in the Artemis experiments, using a standard configuration VMI spectrometer following the Eppink and Parker design[25]. A molecular beam was generated through the expansion of α-pinene in He carrier gas through a 1 kHz pulsed nozzle [26] (Amsterdam Piezo Valve) with a 200 µm aperture. The resulting expansion passed through a 0.75 mm skimmer and entered the interaction region of the spectrometer through a hole in the centre of the repeller plate of the VMI. The typical pressure in the gas and ionization chamber were 1.3×10^{-5} mbar and 4.1×10^{-6} mbar, respectively, and He backing pressure was typically 0.5 bar. The detector consisted of an 80 mm diameter microchannel plate (MCP) and a phosphor screen, which was imaged using a sCMOS camera. The two-dimensional images were processed and fitted to Legendre polynomial expansions using the pBasex algorithm [27]. For PECD measurements, two images using left then right circularly polarized light were recorded, with 30 minutes acquisition time for each. A difference image (left-right) was formed and processed to extract the odd Legendre polynomial coefficients (Eq. (1)), and hence express the experimental PECD asymmetry, G_{AD}, as defined in Eq. (3) . The sum of the images could similarly be Abel inverted to allow the even angular distribution parameters to be extracted.

At Radboud University, REMPI experiments were carried out with 1R-(+)-α-pinene and (1S)-(+)-3-carene using a dual imaging electron-ion coincidence spectrometer that has been previously described [6,13,23]. In this work molecular beams of the α-pinene and 3-carene samples were generated using 0.5 bar Ne carrier gas expanded through a pulsed nozzle [26] (Amsterdam Piezo Valve) also using a 200 µm aperture. The typical operating pressures were 2.0×10^{-4} mbar in the jet expansion chamber and ~5×10^{-7} mbar in the main spectrometer chamber. Using a VMI setup, the photoelectrons and photoions were projected on to time-sensitive delay-line detectors, making

the coincidence analysis possible. In this case, for each PECD measurement, the polarization of light was changed every four hours over a period of 24 hours resulting in three pairs of LCP/RCP images. Photoelectron angular distribution parameters could then be obtained from the electron images using the pBasex code [27] as described above. However, in this case it is now first possible to filter the electron images by selecting the coincident ion mass. In this way mass-tagged electron images can be supplied to the Abel inversion, providing additional selectivity in the data analysis.

Computational

Vertical excitation energies and one- and two-photon transition strengths were estimated by time-dependent density functional theory (TDDFT) implemented in the Gaussian 16 [28] and DALTON [29] programmes. These calculations used the range-separated CAM-B3LYP functional [30] with d-Aug-cc-pVDZ basis functions to identify the excitations from a B3LYP/cc-pVTZ optimized neutral molecule geometry. The energies, transition strengths, and characterization of the electronically excited states are summarized in Tables 2 and 3. These results were validated by repeating the basic TDDFT calculations with various other basis sets including the larger d-Aug-cc-pVTZ. These latter showed only small 0.32±0.09 % (carene) or 0.2±0.1% (α-pinene) shifts in the returned excitation energies and, similarly, other changes (transition strengths, spatial extents etc.) were insignificant for present purposes.

Higher level EOM-CCSD calculations provide some additional clarification in the case of α-pinene. Because of its $O(N^6)$ scaling, for molecules of the size of these terpene $C_{10}H_{16}$ isomers this approach can become prohibitively expensive with a doubly augmented atomic basis, which we deem essential for Rydberg state calculations. Consequently, we have evaluated a basis set which we designate as cc-pVDZ+R, comprising *un*-augmented cc-pVDZ atomic functions, with diffuse functions only placed at the molecular centre of mass. For the latter we used the prescription of Kauffmann[31] to generate a set of *s, p, d, f* Rydberg-like functions ranging up to n=4½ (n=4 for *f*). The performance of this basis, in comparison with a standard d-Aug-cc-pVDZ atomic basis, has been evaluated by calculations made for α-pinene and the similarly sized molecule fenchone. TDDFT calculations return very similar results, but with a substantial reduction in the numbers of basis functions (528 → 309). Such comparisons were also possible for EOM-CCSD calculations but only when limiting the calculation to obtain excitation energies only (that is excluding more expensive properties and transition strengths), but again, excellent agreement was obtained in this more restricted comparison of excitation energies. Consequently, we are confident to extend to full EOM-CCSD/cc-pVDZ+R calculations which, with the smaller basis, no longer exceed available computational resources. We summarise these basis set comparisons for α-pinene in Table 4, and the full EOM-CCSD/cc-pVDZ+R are presented in Table 5.

Results and Discussion

3-Carene

The VUV absorption spectrum [32] of 3-carene is shown in Figure 1. The 3*s* oscillator strength, indicated at the calculated vertical excitation in this figure, is very weak relative to that for the 3*p* and higher Rydberg states, so that this region at the onset of the VUV absorption is very indistinct. The two-photon 3*s* cross-section is more favourable and consequently we include a (2+1) REMPI

spectrum, recorded with a ps laser [33], that provides some additional definition in this region of low Rydberg excitation.

Since the molecular core of the Rydberg states is essentially the ground state cation, we expect the Rydberg and cation potential surfaces will lie parallel and so support very similar vibrational structure. One can then anticipate a Δv=0 propensity rule in ionization of the Rydberg state. Correspondingly, the Franck-Condon (FC) factors for reaching vibrationally excited Rydberg states from the ground state are expected to closely resemble those for direct photoionization. From this understanding, an assignment of the Rydberg absorptions is attempted in Fig.1. Starting from the TDDFT calculated vertical excitation energies, the slow photoelectron spectrum (SPES) for direct VUV ionization of 3-carene into the ground ionic state [34] is taken to provide an estimate of the FC envelope for the ground – 3*s* Rydberg excitation, and is placed at the calculated vertical excitation energy. This is repeated at the commencement of the 3*p* and 3*d* excitation regions. The vibrational structure in the partial simulation so achieved matches observed structure in the experimental spectra, and this matching is further optimized by offsetting all the calculated excitation energies by -0.15 eV. This empirical energy shift is within the expected accuracy of a TDDFT Rydberg calculation.

Figure 2 shows the experimental photoelectron spectra (PES) recorded at 407 nm and 400 nm. Under the conditions employed here we observe some moderate fragmentation in the ion time of flight (ToF) spectrum, with the m/z 93 fragment having ~20% of the parent ion intensity (see, for example the 407 nm ToF, Fig. S1, Supplementary Material). The photoelectron spectra shown in Fig. 2 were recorded in coincidence with parent ion only. Nevertheless, no difference was observed in the fragment ion tagged PES, and we infer that fragmentation takes place *after* ionization. Making the assumption of a (2+1) REMPI process, the recorded electron kinetic energies have been converted to the ionization energy scale plotted in Fig. 2 by subtraction from the three-photon equivalent energy (Table 1). To help identify vibrational structure, the cation HOMO SPES and single photon PECD recorded with 9.5 eV synchrotron radiation are plotted for comparison in the upper panel of Fig. 2. A discussion of the complex SPES vibrational structure has been given elsewhere [35], but here we simply label the prominent vibrational structures as "*v*=0" etc, serving as convenient shorthand for discussing the increasing levels of vibrational excitation.

The two photon excitation at 400 nm is expected to overlap promotion to both a low ("v=0") vibrational level of the 3*p* Rydberg state and a high vibrational level "*v*=3" in the 3*s* Rydberg region (see Fig. 1). Assuming a Δv=0 propensity holds for the subsequent ionization step, these levels map very directly against the same cation vibrational levels that are prominent in the SPES (Fig. 2). The two different intermediate Rydberg states, 3*s* and 3*p* that are thus inferred are marked against the respective PES peaks in Fig. 2, while a schematic representation illustrating the excitation processes is given in Figure 3.

In the 407 nm PES the lower energy "*v*=0" peak at ~8.4 eV is largely suppressed due to the expected poorer overlap of the laser excitation bandwidth with the 3*p* states (Fig. 1). The available excitation energy in the 3*s* state is also reduced at the longer wavelength, and the corresponding Δv=0 PES peak, accessed via the 3*s* intermediate, shifts to slightly lower ionization energy (reduced vibrational level in the cation). This shift of ~0.12 eV exactly matches the reduction in the two-photon equivalent energy between 400 nm and 407 nm (Table 1), providing some corroboration for the (2+1) REMPI mechanism.

Figure 2 also includes the measured MP-PECD asymmetry at 400 nm and 407 nm, plotted to correspond to each PES. Ionization via the vibrationally excited 3*s* intermediate generates a strong chiral asymmetry in the photoelectron angular distribution, rising from around 10% at 407 nm to more than 20% at 400 nm. A much smaller MP-PECD asymmetry factor is observed for the vibrationless 3*p* intermediate ionization at 400 nm, and this asymmetry now lies in the opposite (forward scattering) direction. A single-photon PECD measurement [35] is included in the upper panel of Fig. 2, recorded with a VUV photon energy of 9.5 eV. Although this is a little higher than the 400 nm three-photon equivalent energy of 9.3 eV a comparison with the MP-PECD results is not unreasonable. So while the final states ("*v*=0", "*v*=3" of the $\tilde{X}$ state cation) are the same for single- and multi-photon ionizations, PECD and MP-PECD asymmetry factors are strikingly different, highlighting the importance of the intermediate state in the latter.

More insight into the chiral asymmetry evident in the MP-PECD can be obtained by decomposing G_{AD} into the individual chiral (odd) angular distribution parameters. Such values for the 400 nm REMPI are shown in Figure 4. The b_5 parameter is rather noisy but across the two identified PES peaks, at least, it remains essentially zero. So too does the b_3 parameter in the vicinity of the 3*s* intermediate ionization. However, for the 3*p* intermediate ionization we find $b_3 \approx +0.04$, which is commensurate with the b_1 coefficient in this region. Both b_1 and b_3 thus indicate a significant chiral asymmetry for ionization via the 3*p* Rydberg state, although this chiral response is downplayed when considering $G_{AD,}$ the simple photoelectron asymmetry integrated over the forward and backward facing hemispheres. This is seen in Eq. (3) relating G_{AD} and the b_j parameters , where the sign relationship means that contributions made by the b_1 and b_3 terms partially cancel out. In contrast, the much larger G_{AD} for the 3*s* intermediate peak is seen (Fig. 4) to be almost solely attributable to the significant b_1 parameter ($\approx$ -0.1) in this region, indicating a simple $\cos\theta$ form to the photoelectron angular distribution.

Time-resolved MP-PECD experiments [19] have shown that b_3 parameters may be reduced by rotational dephasing because it gradually destroys the Rydberg state alignment prior to ionization. The electron angular distribution then regresses towards that of a randomly aligned target species with, ultimately, only a single non-zero b_1 parameter expected. Another factor that may be considered as causing a possible reduction of the anticipated two-photon alignment is saturation in the (2+1) REMPI process. However, a systematic study made with camphor (2+1) MP-PECD images [16] found no variation, interpreted as no evidence of saturation, over an intensity range of 2×10^{12} – 12×10^{12} W cm^2. For the electron-ion coincidence imaging results reported here the laser intensity was in any case restricted to less than 2×10^{12} W cm^2 so as to limit ionization to < 0.1 events per laser shot (avoiding false coincidences). For non-coincidence mode detection the maximum intensity used (6×10^{12} W cm^2) remains comfortably withing the above range. More pertinently, we recorded ion mass-selected laser intensity dependences for 3-carene around these intensities (see example in Fig. S2 Supplemental Material). From log-log plots of ion count versus laser intensity we find a linear slope of 2.5$\pm$0.1 for the parent ion and 3.0$\pm$0.1 for the principal m/z 93 fragment. While the parent ion dependence is less than the idealized limit of 3.0 for a fully unsaturated (2+1) REMPI process, in practice some reduction from this limit should be expected as the parent ion yield is competitively depleted at higher laser powers by its increasing subsequent photofragmentation. There is also some reduction in the measured power law expected that is attributable to increasing effective ionization volume as the intensity rises. We thus are reasonably confident that any saturation effects are only minimal.

In Figure 5 we examine the *even* (non-chiral) photoelectron angular distribution parameters determined in the 400/407 nm REMPI processes. At either wavelength, the $b_4^{(\pm1)}$ and $b_6^{(\pm1)}$ terms in the region of the previously identified peaks are not significantly different from zero. On the other hand, the second order term $b_2^{(\pm1)} \approx 0.45$ and shows no discernible variation with either wavelength or with the electronic/vibrational states in the REMPI process. This is quite different from the *odd* (chiral) angular distribution terms which, as seen in Figs. 2 & 4, do so vary.

In the case of a one-photon ionization the $b_2^{(\pm1)}$ term, measured with circularly polarized light, is related to the linear polarization measurement, $b_2^{(0)}$, by $b_2^{(0)} = -2b_2^{(\pm1)}$; $b_2^{(0)}$ is perhaps more widely recognized as β, the photoelectron anisotropy parameter. In this multiphoton case, with the higher order terms being zero, we can make the same identification, suggesting an effective β-parameter of ~0.9. This would indicate a reasonably "parallel" angular distribution with electrons emitted along the electric vector, and as such is not surprising. In an atomic picture one would, however, expect the angular distribution of a $3s^{-1}$ and $3p^{-1}$ photoelectron to differ. A simple atomic-like view of such low Rydberg states is clearly not sustainable, not least because it would also rule out the strong photoelectron sensitivity to the chiral molecular core evidenced by the MP-PECD asymmetries.

α-Pinene

Figure 6 presents a VUV absorption spectrum of α-pinene [36] and a proposed assignment using TDDFT calculations of the vertical Rydberg excitation energies and experimental photoelectron spectra to simulate the possible vibrational envelopes, as described for the 3-carene results. The calculations indicate that although the VUV single photon absorption of α-pinene is weak, the two-photon resonant transition strength for REMPI ionization increases relative to the 3*p* absorptions. Positions and widths of the 407 nm and 400 nm two-photon excitation wavelengths used below are indicated similarly as in Fig. 1, with two additional fs laser lines at 396 nm and 371 nm.

We draw attention to the prominent (one-photon excited) transition predicted at 6.2 eV (6.35 eV before applying offset) that appears to coincide with the 400 nm laser line. Although the VUV absorption spectrum has a maximum in this region, there is no compelling evidence for this individual transition in the spectrum. The TDDFT calculation (Table 3) indicates this state may have some mixed Rydberg-valence π^* character, but its spatial size, $\langle r^2 \rangle$, remains very much the same as the adjacent pure 3*p* Rydbergs. In contrast, the EOM-CCSD calculations (Table 5) provide, a less ambiguous identification as a mixed Rydberg- π^*valence state which is also shifted to be relatively closer to the 3*d* states' energy. Further supporting this, the calculated spatial extent of the excited state is now much more consistent with a valence character, being significantly smaller than any of the clearly identifiable n=3 Rydberg states. Finally, we note that while the single photon oscillator strength is calculated to be at least 2–3 times greater than those of its near neighbours, as appears in Fig. 6, the cross-section estimated for its circularly polarized two-photon excitation are a factor 2–3 *smaller* than the adjacent 3*p* Rydberg excitations. The greater valence character of this state may also cause there to be more efficient, rapid relaxation pathways that could further suppress any contribution to the (2+1) REMPI spectrum. Overall, we conclude from the EOM-CCSD calculation that this transition is shifted well above the 400/396 nm laser excitations and that Fig. 6 visually

exaggerates both the position and prominence of this transition for the REMPI measurements. In the absence of experimental evidence, we therefore discount its role.

The resulting photoelectron spectra recorded for the four laser excitation energies are shown in Figure 7.

The 407 nm α-pinene REMPI PES result can be discussed in a manner closely paralleling that for 3-carene, while noting that the laser now slightly exceeds the 3p threshold, suggesting better overlap with, and possibly some modest vibrational excitation of, the 3*p* intermediate (Fig. 6). With additional support derived from comparison with the α-pinene SPES (also included in Fig. 7), the stronger and slightly broader peak at ~8.2 eV can be identified as Δv=0 ionization via the threshold region of the 3*p* Rydberg states. As before, the 8.7 eV peak can be identified as ionization via the vibrationally excited "*v*=3" 3*s* Rydberg intermediate.

The 400 nm result also largely parallels that discussed for 3-carene. The 3*s* intermediate peak shifts to slightly higher ionization energy, 8.8 eV, as the shorter wavelength now weakly excites via an even more vibrationally excited ("*v*=3+") intermediate level. Similarly, the assigned 3*p* PES peak shifts to ~8.3 eV as it also acquires some modest vibrational excitation in the intermediate excitation.

The 407 nm and 400 nm spectra were recorded, as before in electron-ion coincidence mode. Compared to 3-carene the fragmentation we observe in the ion ToF mass spectrum is a little more extensive (Fig. S3 Supplemental Material), with the dominant m/z 93 fragment reaching ~50% of the parent ion yield at 400 nm. However, the laser power dependence of both the parent and m/z 93 fragment (Fig. S4 Supplemental Material) were found to be identical to that of the 3-carene, and we make the same inference that any effects of saturation in the (2+1) REMPI process may reasonably be ignored for present discussion. Also, as before, we examined the fragment- and parent-ion mass tagged electron spectra, but observed no significant difference. Again, we infer that the observed fragmentation follows the ionization, but for better statistical quality fragment and parent coincident data are combined in the results presented here.

The 396 nm and 371 nm spectra were recorded without coincident ion detection, and so without requiring the count rate limitation imposed by that recording mode. The estimated laser intensity employed at 400 nm (1×10^{12} W cm^{-2}) is doubled for the 396 nm measurement, but increases to ~6×10^{12} W cm^{-2} for the 371 nm electron imaging. The higher count rates provide improved S/N in the corresponding VMI images. Otherwise, the 396 nm PES spectrum is very similar in appearance to that recorded at 400 nm. Closer examination in fact reveals that neither of the two prominent peaks is shifted toward higher ionization energy, as may be expected given the shorter wavelength excitation. For the 3*p* intermediate this is possibly because the excitation laser now overlaps favourably with an electronically more excited 3*p* sub-state, with correspondingly lower vibrational excitation.

Last, we turn to examine the 371 nm PES. Given the substantial increase in excitation energy, this may first appear surprisingly similar to the 396 nm PES, having the same cation vibrational peaks (albeit with differing intensity ratios). However, Fig. 6 now very strongly suggests that the vibrationless ~8.2 eV PES peak corresponds to excitation via the near threshold region of the 3*d* states, with now the ~8.8 eV peak arising from excitation of a "v≈3" 3*p* Rydberg. Referring again to the REMPI schematic Fig. 3, and assuming essentially identical vibrational level spacing in all

electronic states being considered, it can be seen that the energetic separation between photoelectron peaks should be essentially the electronic energy gap between the competing Rydberg excitations. The numerical calculations in Table 3, do indeed show 3*s* — 3p_3 and 3p_3—3*d* separations that are commensurate with experimental ~0.55 eV PES peak separations at 396 nm and 371 nm.

Finally, we observe that the 371 nm spectrum in Fig. 7 shows a third weak peak at ~9.25 eV whose presence is reinforced when the $b_2^{(\pm 1)}$ photoelectron angular distribution parameters, also plotted in Fig. 7, are examined. At all four wavelengths examined these 2nd order anisotropy parameters reach minima at the identified peak positions in the <9 eV region, returning towards zero elsewhere. A clear dip of the $b_2^{(\pm 1)}$ coefficient ~9.25 eV in the 371 nm PES is likewise evident. This ionization energy is well outside the feasible window for vertical excitation/ionization from the ground state π orbital. In fact, comparison with the VUV SPES (Fig. 7) places the ionization in the threshold region of the electronically excited *A* state cation.

The simplest explanation to advance would be an independent electron model of ionization occurring from an intermediate Rydberg state having an excited *A* state cation core. The 15th excited state predicted by TDDFT calculations (Table 3) results from a HOMO-1 $\rightarrow$ 3*s* Rydberg excitation at 7.25 eV (7.10 eV with our empirical plotting offset). While the reliability of TDDFT results may be questioned at this level of excitation, the EOM-CCSD calculations (Table 5) identify the same transition, with the same vertical excitation energy. In both calculations the reduced spatial extent $\langle r^2 \rangle$ for the Rydberg state helps corroborate its 3*s* identity. The shape of the *A* band SPES (Fig. 7) indicates that its onset and adiabatic ionization energy extends some 0.5 eV lower than the vertical ionization. Hence it is energetically entirely feasible that a two photon 371 nm excitation pulse ($\equiv$6.7 eV) would partially overlap the low energy onset of the corresponding excited core 3*s* Rydberg state absorption.

Figure 8 shows the MP-PECD results obtained for α-pinene at these four photon energies. Considering the 407 — 396 nm spectra it is apparent that there are key similarities. Note that the 396 nm measurement uses the 1S-(-) enantiomer, but for ease of comparison the plot axis has been reversed to visually accommodate the expected G_{AD} asymmetry flip associated with switching enantiomer. The MP-PECD associated with the peak that has been assigned as proceeding via a vibrationally excited 3s intermediate state has a consistently small magnitude <0.03. In contrast, there seems a much larger G_{AD} asymmetry associated with REMPI via a near threshold 3p intermediate. At 407 nm the suggested 3p REMPI-PES peak has a profile that suggests a splitting around the 8.21 eV first vertical ionization energy seen in the SPES, and correspondingly G_{AD} approximately doubles between the high and low energy sides. This would seem to correspond to two vibrational excitations, the lower energy one falling at the estimated adiabatic ionization energy of 8.16 eV [34]. While the 3p intermediate peak of the 396 nm REMPI-PES does not obviously resolve into two vibrational components, the MP-PECD displays the same step function around the 8.21 eV vertical ionization energy that naturally suggests the presence of two underlying vibrational components.

A complete set of photoelectron angular distribution parameters, b_1–b_6 (Eq. (1)), measured for the 396 nm REMPI, are shown in Figure 9. The odd, chiral, parameters are displayed in the upper panel. As already noted, the overall MP-PECD associated with the 3*s* intermediate ionization (~8.8 eV), is

small and it is evident that the individual contributions here are themselves small. However, all three odd parameters have a significant non-zero magnitude around the 3*p* ionization (~8.2 eV), with b_3 having the largest magnitude. The set of even parameters (lower panel) have $|b_2|$ larger than b_4, while the noisier highest order b_6 term does not differ significantly from zero in the vicinity of the two peaks.

In accordance with Yang's theorem [10] the photoelectron angular distribution, Eq. (1), for ionization of an initially randomly oriented sample would be limited to no more than the 2nd Legendre polynomial term; the significant presence of terms up to the 5th order polynomial is a clear indication that at least three photons are absorbed, contributing their angular momentum to the net anisotropy in the process. For the assumed (2+1) REMPI mechanism, a two-photon resonant intermediate excitation is supposed to be followed a single photon ionization of the intermediate. Additional anisotropy for the latter photoemission step comes from preferential molecular axis alignment in the excited intermediate. Theoretical models that attempt to capture such a two-photon induced intermediate alignment have proven to offer a semi-quantitative account of experimental MP-PECD results in the case of camphor [14] and fenchone [37]. The current results for α-pinene, with very substantial b_3–b_5 coefficients that cannot be present in the photoionization of a randomly oriented intermediate state, presents as a very strong test-case for further refinement of theoretical treatments.

Concluding this discussion, we provide in Figure 10 a comparison of the 396 nm MP-PECD (three-photon equivalent energy 9.38 eV) with a previous synchrotron experiment recording the PECD at a similar photon energy of 9.5 eV [34]. Allowing for the sign flip caused by the use of different enantiomers in these particular experiments, it can be seen that the overall trend of decreasing magnitude with increasing ionization energy is similar, but that the magnitude of the photoelectron chiral asymmetry in the synchrotron experiment is a factor of 3–4 greater than in the multiphoton excitation.

Summary

Femtosecond laser (2+1) REMPI with VMI detection of the photoelectrons has been used to examine the full set of the resulting photoelectron angular distribution parameters, b_j, up to the limit *j*=6 set by the Yang theorem[10] for a net three-photon process. We include the odd chiral coefficients, *j*=1,3,5, in this determination by using circular polarization of the light, and enantiopure samples of our chosen chiral target molecules, 3-carene and α-pinene. Hence, we express and discuss these chiral results as multiphoton photoelectron circular dichroism (MP-PECD). Our studies span up to four different excitation wavelengths that permit different two-photon resonant intermediate states to be selected, while the REMPI photoelectron spectra simultaneously reveal details of the final cation electronic and vibrational level.

The Rydberg levels excited in the two-photon resonances are first identified using a combination of VUV absorption spectra, theoretical calculations of the vertical excitation energies, and partial vibrational simulations. Assuming parallel vibrational potentials of the cation and the Rydberg state's molecular core, these simulations use experimental PES recorded for the direct VUV ionization to approximate the anticipated vibrational structure and bandwidth of a single Rydberg level. In practice this assumption is justified by our observation of a strong Δv=0 propensity in the REMPI PES.

For REMPI ionization of both molecules the $b_2^{\{\pm1\}}$ parameter dominates the even Legendre coefficients, the direction corresponding to a "parallel" emission with linear polarization. Perhaps surprisingly, for 3-carene this result seems independent of whether a 3*s* or 3*p* intermediate state is accessed. For α-pinene, the photoemission remains "parallel", but with more variation between intermediate levels.

In contrast, the MP-PECD (odd Legendre terms) displays a great sensitivity to the selected intermediate state. G_{AD}, the chiral asymmetry, is large (up to ~20%) for the 3-carene 3*s* intermediate, but much smaller, and reversed in direction, for the 3*p* intermediate. Nevertheless, an examination of the individual photoelectron angular parameters for the 3p intermediate ionization reveals that, far from seeming to be nearly achiral in behavior, there is a significant chiral anisotropy displayed by b_1 *and* b_3 . The richer angular distribution that this indicates is not fully captured in the simple forward-backward parameterization offered by G_{AD} , as has been previously noted [16]. Of course the final electronic state (cation) is the same for ionization via both 3s and 3p intermediates, and a comparison with the direct PECD recorded with synchrotron radiation at comparable total excitation energies is revealing; while the PECD asymmetry spans the same range, the vibrational dependence (Fig.2) is completely opposed.

For α-pinene, MP-PECD is strongest for the 3*p* intermediate REMPI, but while the comparison with single photon MP-PECD at comparable total energy indicates a similar trend in the asymmetry with vibrational level, the magnitude of the MP-PECD is much reduced. The decomposition of the 396 nm MP-PECD into individual b_1, b_3, and b_5 parameters (Fig. 8) is interesting as the b_3 exceeds b_1 in magnitude, and b_5 is also sizeable in the 3*p* intermediate state ionization. While b_1 still provides the dominant term in the net asymmetry (Eq. (3)) these non-zero higher coefficients terms must necessarily result from photoalignment in the intermediate.

Fenchone provides the most widely studied system against which these MP-PECD results can be compared [15-19,38,39]. The most recent fs laser studies find $|b_1| \approx 6\%$ with $|b_3| \approx 2\%$ and vanishing b_5 values for the 3*s* intermediate in fenchone[16,17,39]. Much smaller values of these coefficients, and consequently the MP-PECD asymmetry, are found in the 3*p* excitation range. Interestingly, ns laser REMPI experiments [18] report only slight differences in MP-PECD between the 3*s* and 3*p* excitation regions, with b_3 as well as b_5 dropping to ~0. The similarity may be ascribed to internal conversion of the $3p \rightarrow 3s$ Rydberg state on the nanosecond timescale of these later experiments, meaning the ionization steps all originate from the 3*s* intermediate. The noted reduction in b_3 may be attributed to a rotational dephasing of the initially photoaligned intermediate with the longer ionization timescales [19] [39], reinforcing an association of the higher order terms with intermediate two-photon alignment when the ionization step is accomplished by a single additional photon. A higher energy four-photon ionization process presents $|b_3| > |b_1|$ as commented on in our α-pinene discussion.

Mostly these considerations have focused on Rydberg states that are generated by ionizing the outermost π valence orbitals, and so possess a molecular core with the configuration of the ground *A* state cation. In both molecules, however, the theoretical predictions include Rydberg state transitions originating from neutral orbitals below the HOMO. These create electronically excited Rydberg cores. Generally, these lie beyond the excitation energies employed, but the 371 nm REMPI of α-pinene is observed to include ionization into the excited *A* state cation that can naturally be associated with one such core excited 3*s* Rydberg state. The α-pinene calculations also suggest a

mixed Rydberg/π* valence excitation between its 3*p* and *3d* regions, although the different calculations disagree on its precise energy. In practice we detect no strong evidence for this state in either the single-photon absorption or REMPI spectra.

Acknowledgements

This research was undertaken as part of the ASPIRE Innovative Training Network, which has received funding from the European Union's Horizon 2020 research and innovation programme under the Marie Sklodowska-Curie Grant Agreement No. 674960. HG and DPS thank Aspire for ESR Fellowships.

Funding for Laser facility access was received from LASERLAB-EUROPE (grant agreement 654148, EU H2020 research and innovation programme) award #LLAMS002376 (IP) for work in Nijmegen, and from the STFC (UKRI) for access to the Central Laser Facility "Artemis" system, award #17220004 (IP and KLR).

RSM thanks the Royal Society for a University Research Fellowship (UF100047, UF150655).

We thank Kevin Schug for providing the 3-carene absorption spectrum data from ref [32] .

The authors gratefully thank Maurice Janssen for his enthusiastic support and suggestions to use the electron-ion imaging apparatus at Nijmegen, and Wybren-Jan Buma for helping facilitate this.

Daniel Horke and Anders Huits are thanked for their help with data acquisition in Nijmegen and Yu Zhang and Adam Wyatt for their assistance at Artemis.

Finally, we thank Dave Parker for welcoming our team to the Institute for Molecules and Materials at Radboud University and ensuring a productive and stimulating visit.

Supplemental Material provides four figures S1–S4 showing example ToF mass spectra and laser intensity dependence plots for 3-carene and α-pinene.

Tables

Table 1

Laser characteristics

λ (nm)	Δλ (nm) [a]	Pulse Characteristics		Polarization Stokes S_3		2-photon Excitation		3-photon
		E (μJ) [b]	Δt (fs)			2×*h*ν (eV)	$\Delta E_{2\phi}$ (eV) [c]	3×*h*ν (eV)
407.05	2.45	23–36	150	+0.98	-0.99	6.09	0.026	9.14
399.88	2.77	23–36	150			6.20	0.030	9.31
396.52	4.24	5-12	50	+0.90	-0.98	6.25	0.047	9.38
371.02	3.93	5–17	50			6.68	0.071	10.02

[a] Measured laser line spectrum bandwidth (FWHM)
[b] Typical value used for measurements
[c] Estimated FWHM of two-photon excitation from convolution of two single photon bandwidths

Table 2

TDDFT CAM-B3LYP/d-Aug-cc-pVDZ calculated vertical electronic excitations for 3-carene at the B3LYP/cc-pVTZ optimized ground state geometry

State No.	eV	f [(a)]	$\langle r^2 \rangle$ (a.u.) [(b)]	$\Delta\langle r^2 \rangle$ (a.u.) [(b)]	$\sigma(2)$ (a.u.) [(c)]	Excitation [(d)]
1	5.79	0.0006	1628	50	30.2	H→3s
2	6.32	0.0301	1640	62	63.2	H→3p
3	6.33	0.0107	1650	71	121.0	H→3p
4	6.44	0.0052	1657	78	30.6	H→3p
5	6.52	0.0164	1630	52	30.8	H-1 →- 3s
6	6.81	0.1409	1647	69	8.7	H→3d(+π*)
7	6.83	0.0013	1652	74	13.7	H-2 → 3s
8	6.90	0.0026	1682	103	18.4	H→3d
9	6.94	0.0177	1691	113	8.8	H→3d
10	6.98	0.0009	1705	126	1.7	H→???
11	7.00	0.0088	1705	127		H→3d
12	7.04	0.0021	1645	66		H-1 → 3p
13	7.11	0.011	1662	84		H-1 → 3p
14	7.16	0.0131	1772	194		H→4s
15	7.19	0.0253	1731	153		H→?3d ?

(a) Oscillator strength (single photon excitation)

(b) Spatial extent of state and its difference from the ground state neutral $\langle r^2 \rangle$ expectation.

(c) Two-photon cross-section for circular polarization

(d) Where possible a simple characterisation of the excited state is listed. The initial orbital excited is the HOMO, except for states 5,12,13 (HOMO-1) and state 7 (HOMO-2)

Table 3

TDDFT CAM-B3LYP/d-Aug-cc-pVDZ calculated vertical electronic excitations for α-pinene at the B3LYP/cc-pVTZ optimized ground state geometry

	eV	f [(a)]	$\langle r^2 \rangle$ (a.u.) [(b)]	$\Delta\langle r^2 \rangle$ (a.u.) [(b)]	σ(2) (a.u.) [(c)]	Excitation [(d)]
1	5.73	0.0005	1436	57	17.1	H→3s
2	6.18	0.0177	1448	69	70.0	H→3p
3	6.21	0.0346	1440	61	39.2	H→3p
4	6.28	0.0285	1440	62	51.7	H→3p
5	6.35	0.0621	1437	58	25.3	H→Ry, π*
6	6.74	0.0084	1485	106	3.4	H→3d
7	6.79	0.0072	1495	116	12.8	H→3d
8	6.81	0.0071	1512	133	15.4	H→3d
9	6.81	0.0089	1510	131	15.7	H→3d
10	6.96	0.0144	1535	156	6.8	H→3d
11	7.00	0.0026	1608	229		H→4s
12	7.17	0.0006	1658	279		H→4p
13	7.20	0.0036	1629	250		H→4p
14	7.23	0.0083	1612	233		H→4p
15	7.25	0.0166	1487	108		H-1 → 3s
16	7.30	0.0014	1589	210		H→4d

(a) Oscillator strength (single photon excitation)

(b) Spatial extent of state and its difference from the ground state neutral $\langle r^2 \rangle$ expectation.

(c) Two-photon cross-section for identical circularly polarized photons.

(d) The simplest characterisation of the excited state is listed. The initial orbital excited is the HOMO, except state 15 where it is the HOMO-1.

Table 4

Comparison of Rydberg state energies (eV) obtained with d-Aug-cc-pVDZ and the reduced size cc-pVDZ+R basis sets, using TDDFT (CAM-B3LYP) and EOM-CCSD methods.

	TDDFT CAM-B3LYP (eV)		**EOM-CCSD (eV)**	
	VDZ+R [(a)]	**dAVDZ [(b)]**	**VDZ+R [(a)]**	**dAVDZ [(b)]**
1	5.73	5.73	5.86	5.87
2	6.18	6.18	6.28	6.30
3	6.22	6.21	6.34	6.35
4	6.29	6.28	6.40	6.41
5	6.37	6.35	6.69	6.62
6	6.73	6.74	6.84	6.84
7	6.78	6.79	6.89	6.91
8	6.80	6.80	6.91	6.93
9	6.81	6.81	6.93	6.94
10	6.92	6.94	7.12	7.14

(a) Calculations with the cc-pVDZ+R basis described in the text.

(b) Calculations with the standard d-Aug-cc-pVDZ atomic basis.

Table 5

EOM-CCSD/cc-pVDZ+R calculated electronic excitations for α-pinene at the B3LYP/cc-pVTZ optimized ground state geometry

	eV	f [(a)]	$\langle r^2 \rangle$ (a.u.) [(b)]	$\Delta\langle r^2 \rangle$ (a.u.) [(b)]	σ(2) (a.u.) [(c)]	Excitation [(d)]
1	5.86	0.0011	1444	63	23.4	H→3s
2	6.28	0.0011	1462	82	59.1	H→3p
3	6.34	0.0044	1460	80	67.8	H→3p
4	6.40	0.0055	1470	89	44.8	H→3p
5	6.69	0.0699	1435	54	21.3	H→ Ry,π*
6	6.84	0.0078	1496	115	6.6	H→3d
7	6.89	0.0111	1509	128	11.5	H→3d
8	6.91	0.0064	1519	138	46.5	H→3d
9	6.93		1524	144		H→3d
10	7.12		1650	269		H→3d
11	7.18		1559	179		
12	7.25		1456	76		H-1→3s
13	7.30		1755	374		

(a) Oscillator strength (single photon excitation)

(b) Spatial extent of state and its difference from the ground state neutral $\langle r^2 \rangle$ expectation.

(c) Two-photon cross-section for identical circularly polarized photons

(d) Excitation from the molecule's HOMO orbital to the characterised Rydberg/valence state, excepting state 12 where the initial orbital is HOMO-1.

Figures

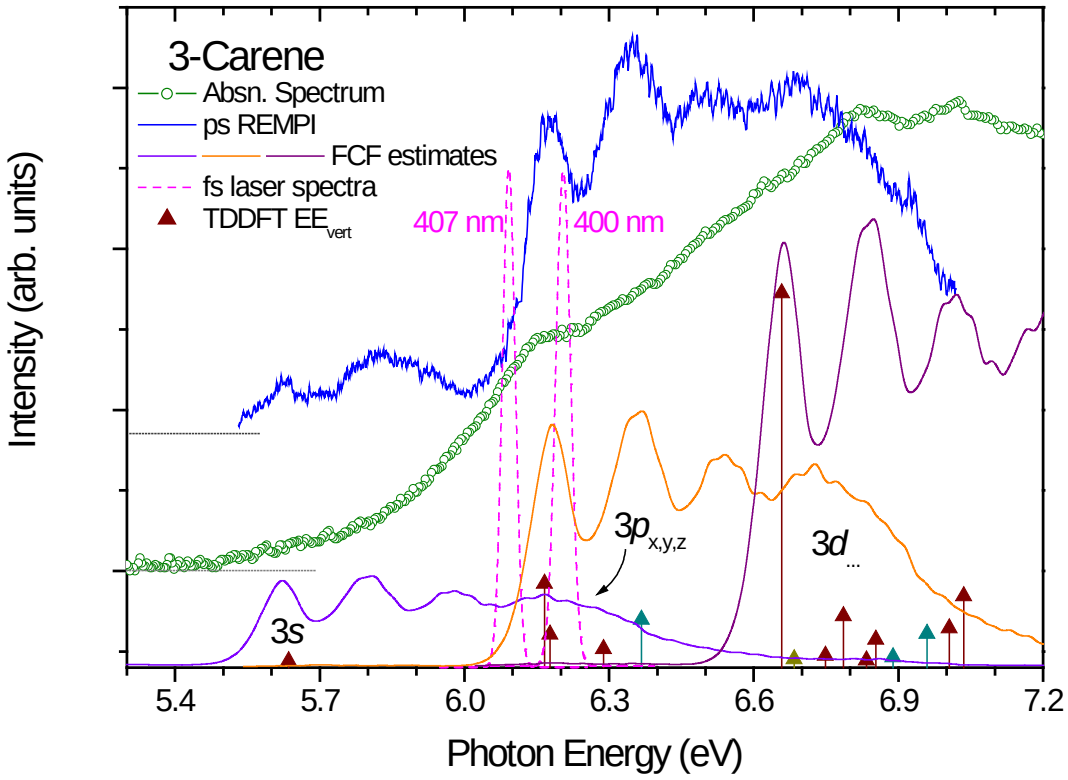

Figure 1.

The VUV absorption spectrum (Ref [32]) and (2+1) ps laser REMPI spectrum (Ref. [33]) in the n=3 Rydberg series excitation region. CAM-B3LYP/d-Aug-cc-pVDZ vertical excitation energies are marked by arrows whose relative lengths reflect the calculated oscillator strengths (single photon excitation). To provide a visual indication of the likely Franck-Condon vibrational envelope of these Rydberg excitations, scaled profiles of the X^+ cation photoelectron spectrum are positioned at the 3*s* and first 3*p* and 3*d* calculated excitations positions, plotted with -0.15 eV offset. Above 6.3 eV 3*s*, 3*p* Rydberg excitations from the HOMO-1 and HOMO-2 orbitals are predicted to be interspersed; these are indicated by cyan and dark yellow arrows respectively. The position of the two-photon excitations we report at 407 nm and 400 nm are marked (dashed lines) with widths corresponding to the convolved laser linewidths.

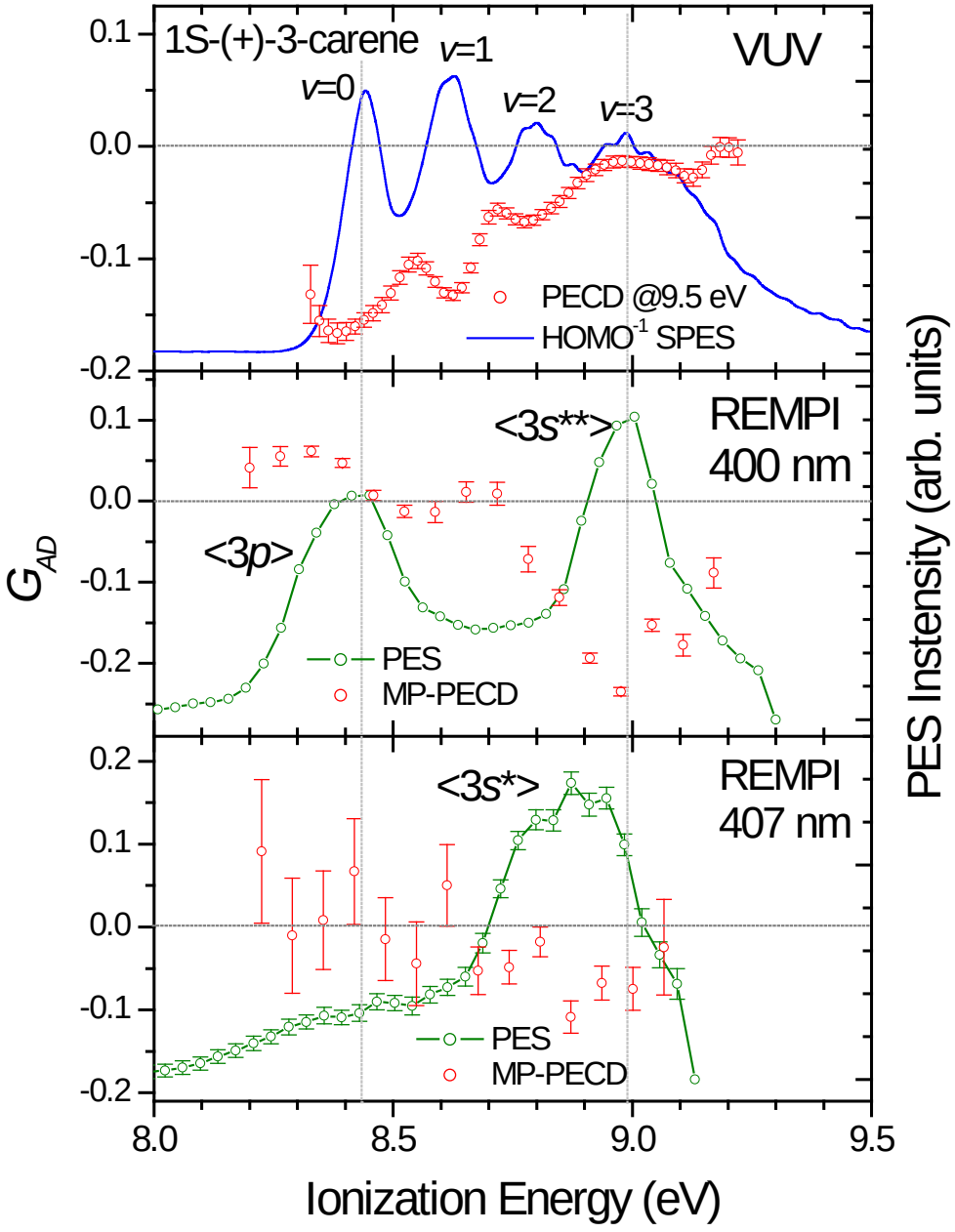

Figure 2

Parent ion mass-tagged REMPI PES and MP-PECD (G_{AD}) spectra for the 1S-(+)-3-carene enantiomer recorded at 400 nm (mid panel) and 407 nm (lower panel). Electron kinetic energies are converted to ionization energy by assuming a net 3-photon excitation (Table 1). In the top panel for comparison we show the VUV SPES for ionization of the HOMO orbital recorded with scanned synchrotron radiation and have overplotted the single photon PECD measured at 9.5 eV (Ref. [35]). Grid lines are drawn to help guide the eye when comparing results. The SPES peak labels (v=0…) are provided purely as a convenience for discussing successive vibrational excitations, but do not signify specific quantum levels.

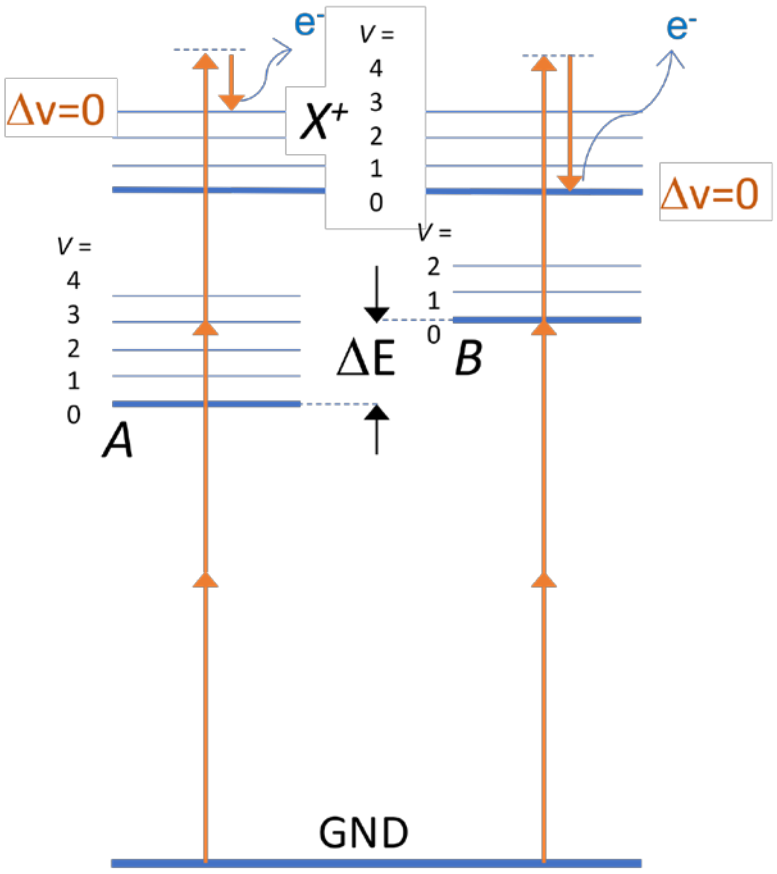

Figure 3

Schematic showing (2+1) REMPI excitation via two alternative Rydberg intermediate states, *A* and *B*, having the same molecular ion core. The common final X^+ state will have a vibrational structure expected to be closely reproduced in each intermediate state, carrying the implication of a Δv=0 vibrational propensity rule. The photoelectron spectrum is then expected to show two vibrational bands (here v=3, v=0) with an energy separation equaling the electronic energy difference between *A* and *B*. In discussion of the 407 nm — 396 nm measurements, state *A*, can be understood as a 3*s* Rydberg, state *B* as a 3*p* Rydberg. For the 371 nm excitation these should instead be, respectively, 3*p* and 3*d* Rydberg states.

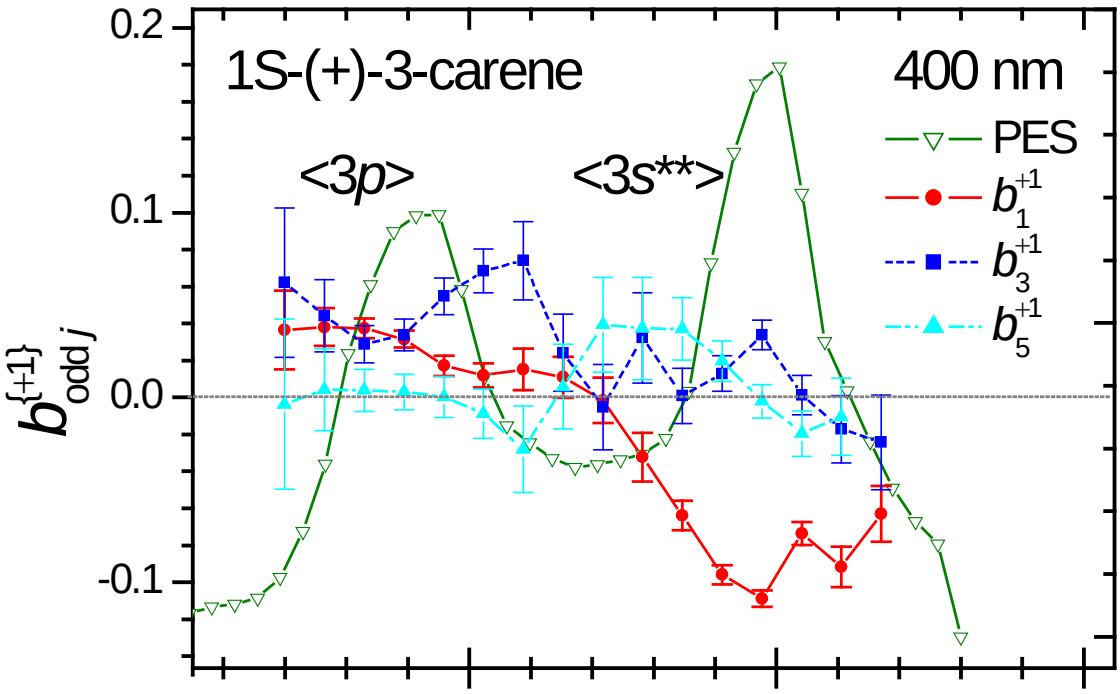

Figure 4

Individual chiral (odd) angular distribution parameters ($b_1^{\{+1\}}, b_3^{\{+1\}}, b_5^{\{+1\}}$) and photoelectron spectrum measured for the 400 nm REMPI ionization of 1S-(+)-3-carene enantiomers. The data are filtered in coincidence with parent (m/z 136) ion masses. The REMPI-PES peaks are labelled to indicate the intermediate state as discussed in the text and shown in Fig. 2.

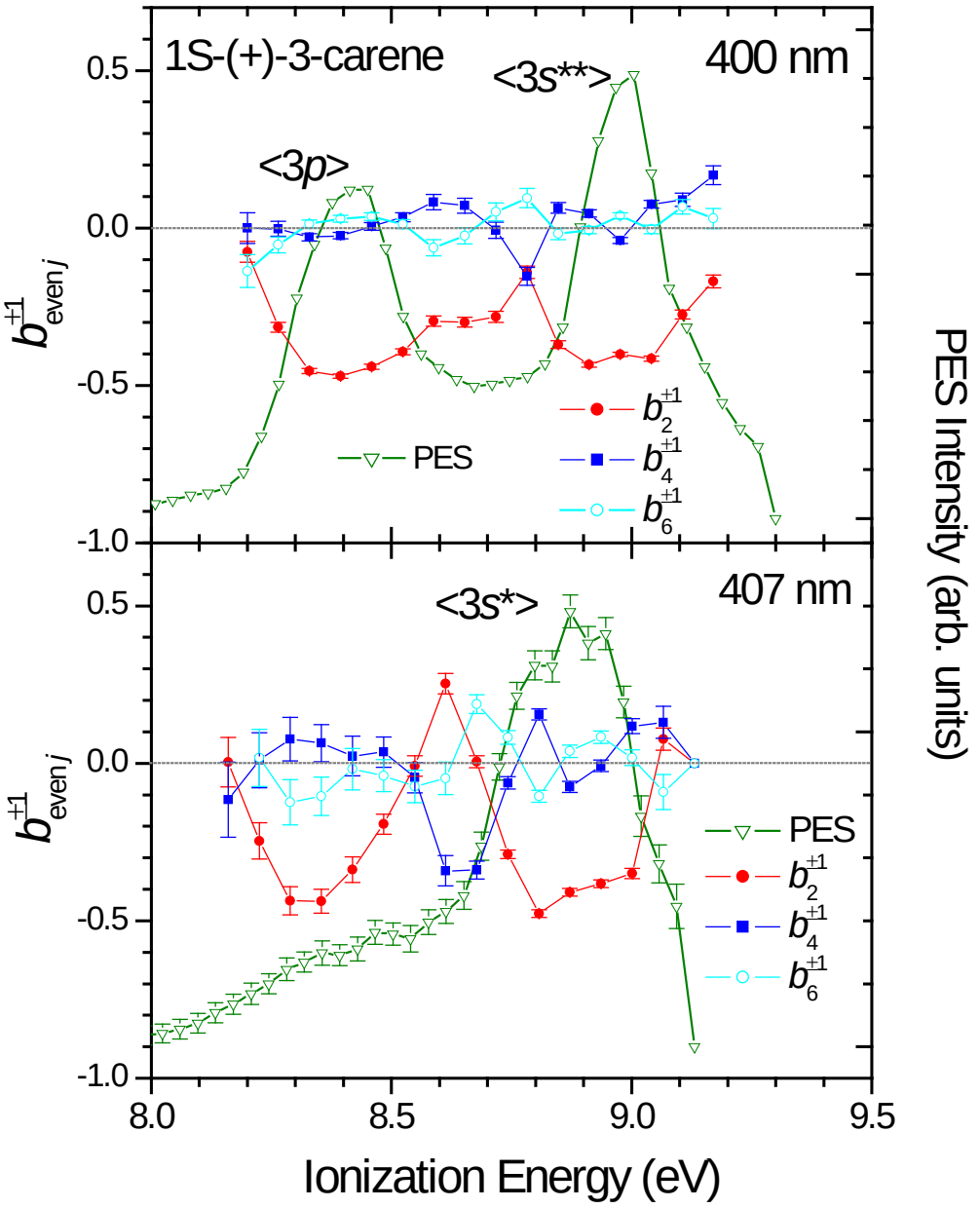

Figure 5

3-Carene REMPI PES and the even photoelectron angular distribution parameters, $b_2^{(\pm1)}, b_4^{(\pm1)}, b_6^{(\pm1)}$. The data are filtered in coincidence with parent (m/z 136) ion masses.

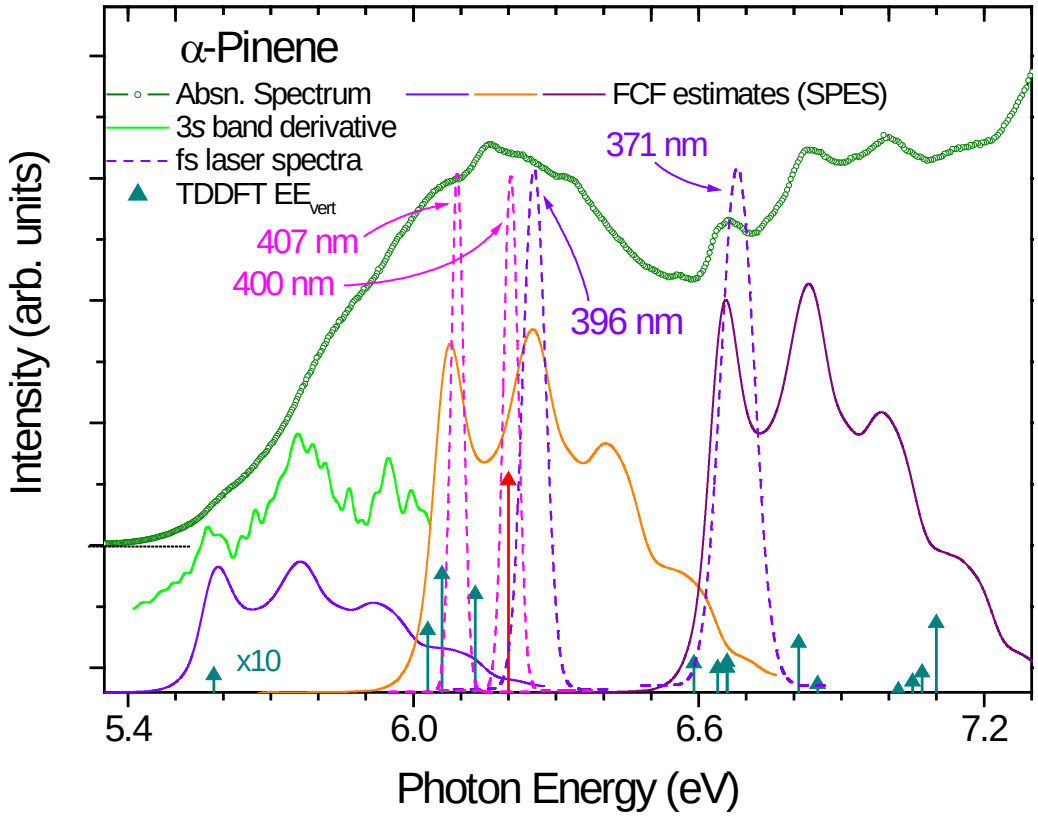

Figure 6

The VUV absorption spectrum of α-pinene (from Ref. [36]) A partial simulation, as described for Fig. 1, is attempted by positioning the experimental FC envelope (SPES) for direct ionization at the 3*s*, 3*p*, and 3*d* onsets identified by CAM-B3LYP/d-Aug-cc-pVDZ TDDFT calculation. Weak and very weak shoulders of the 3*s* vibrational structure may be discerned in the spectrum, but are better identified from the included numerical differentiation of this spectral region. The overall alignment with the experimental structures is again optimized by offsetting calculated vertical excitation energies by -0.15 eV. The fs laser two-photon energies and widths used for this study (Table 1) are marked with dashed lines.

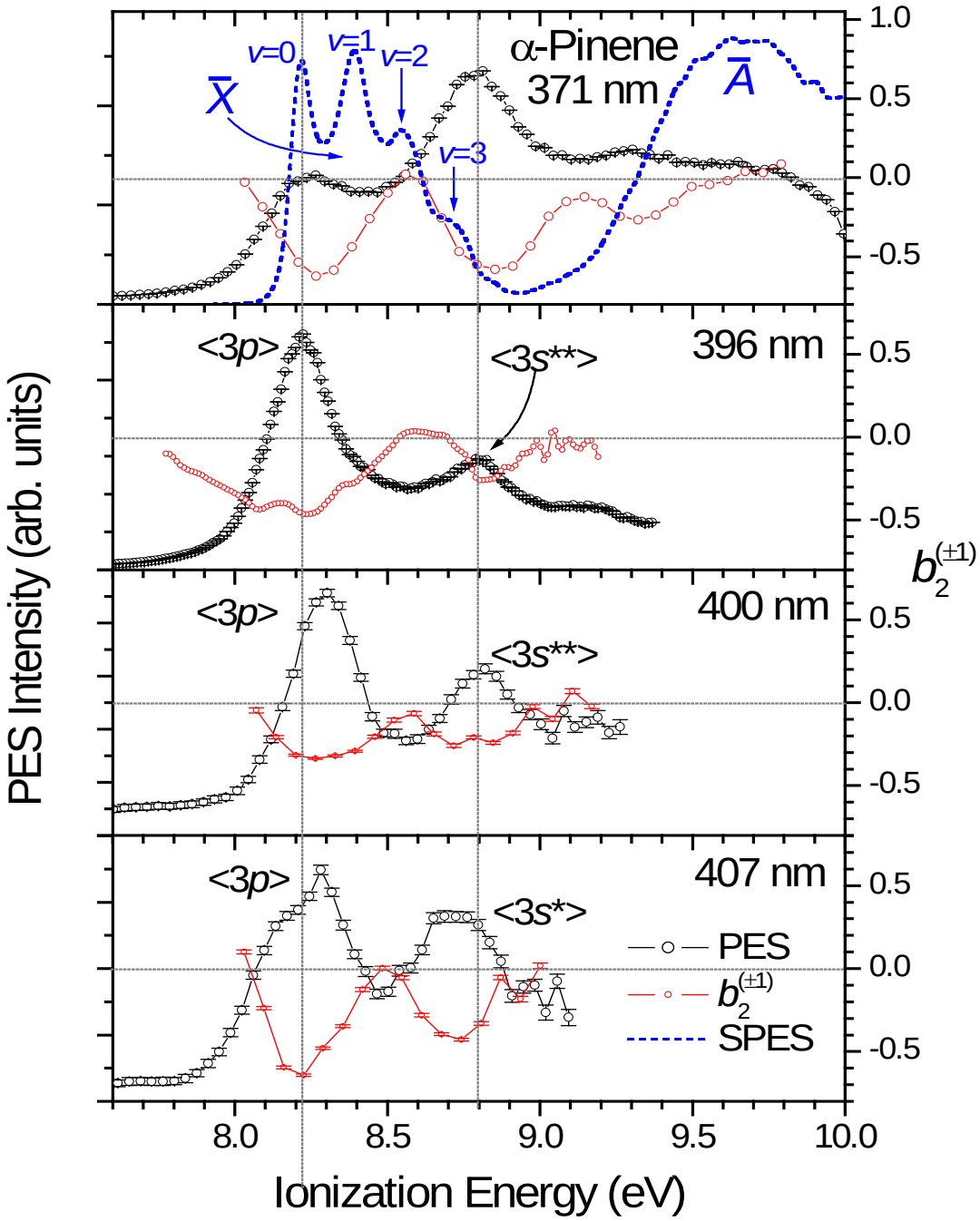

Figure 7

REMPI PES spectra for α-pinene recorded at the indicated laser wavelengths. Filtering by coincident ion selection accepts both parent (m/z 136) and major fragment (m/z 93) mass peaks. Also plotted on the same ionization energy scale are the 2nd order anisotropy parameters, $b_2^{\{\pm1\}}$, recorded using circularly polarized radiation. In the top panel we show, for comparison, the first and second ionization bands of a VUV SPES recorded with scanned synchrotron VUV radiation[34]. Grid lines are drawn to help guide the eye when comparing results. Other detail as for Fig. 2

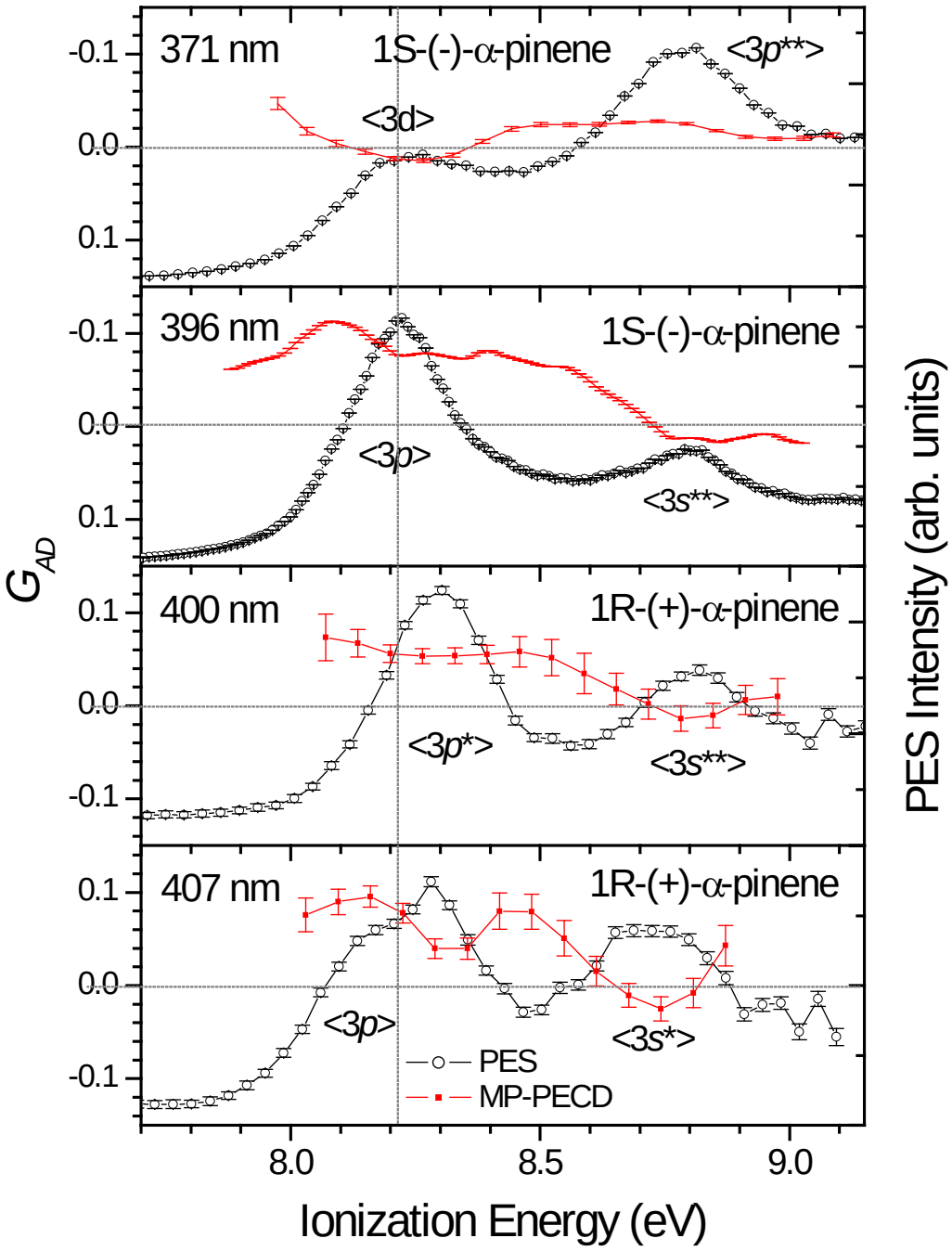

Figure 8

MP-PECD measurements for α-pinene recorded at four different laser wavelengths (as indicated in the figure). Note the different enantiomer used in top two panels. To accommodate an expected switch in the chiral asymmetry accompanying an enantiomer switch while facilitating visual comparison, the plotting inverts the MP-PECD axes in these panels. Ionization energies are established from the measured electron kinetic energy by assuming a net 3-photon excitation. The corresponding REMPI PES (Fig. 7) are also repeated in these panels to assist in identifying correlations with deduced intermediate and vibrational levels. The indicated peak assignments to intermediate states are as discussed for Fig. 7

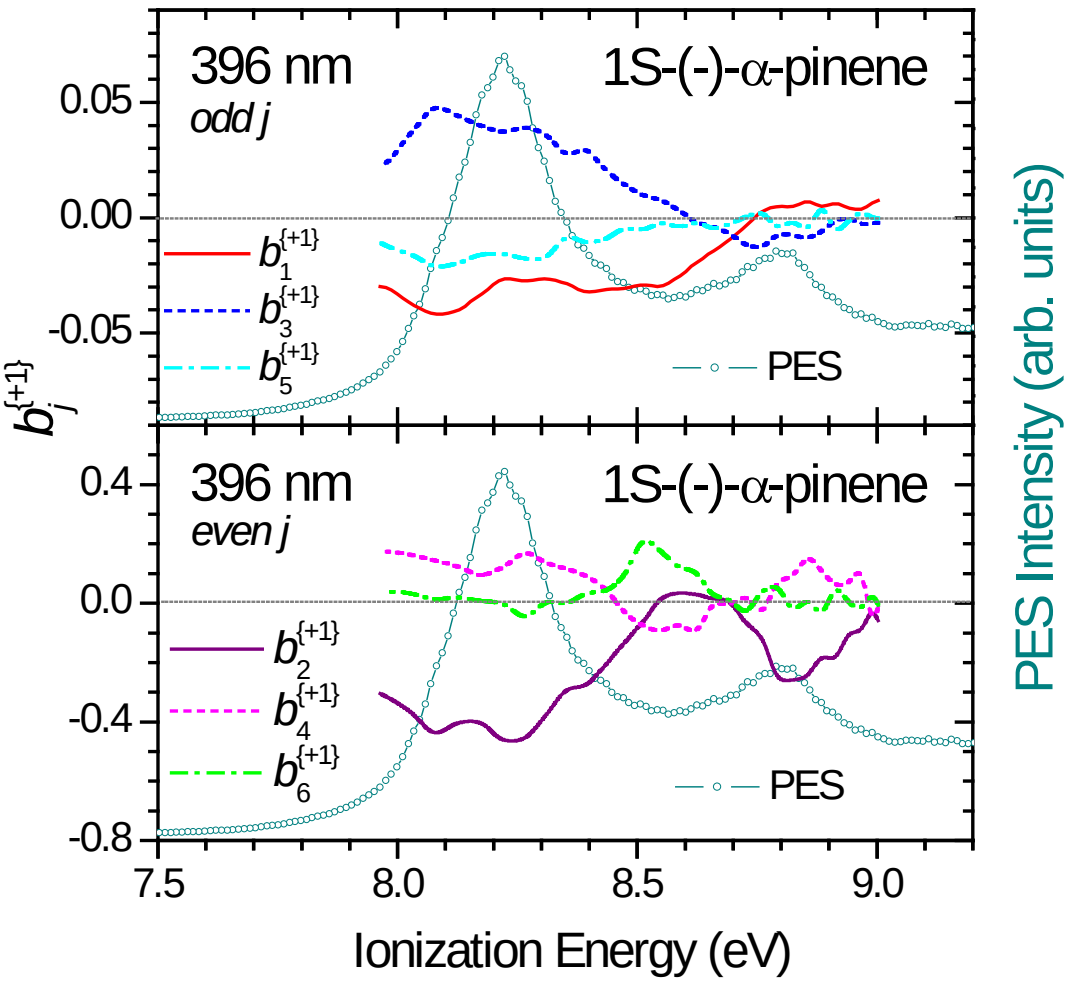

Figure 9

Photoelectron angular distribution parameters b_1 – b_6 for the ionization of 1S-(-)-α-pinene using circularly polarized 396 nm laser REMPI. Also included in the two panels for comparisons is the REMPI-PES

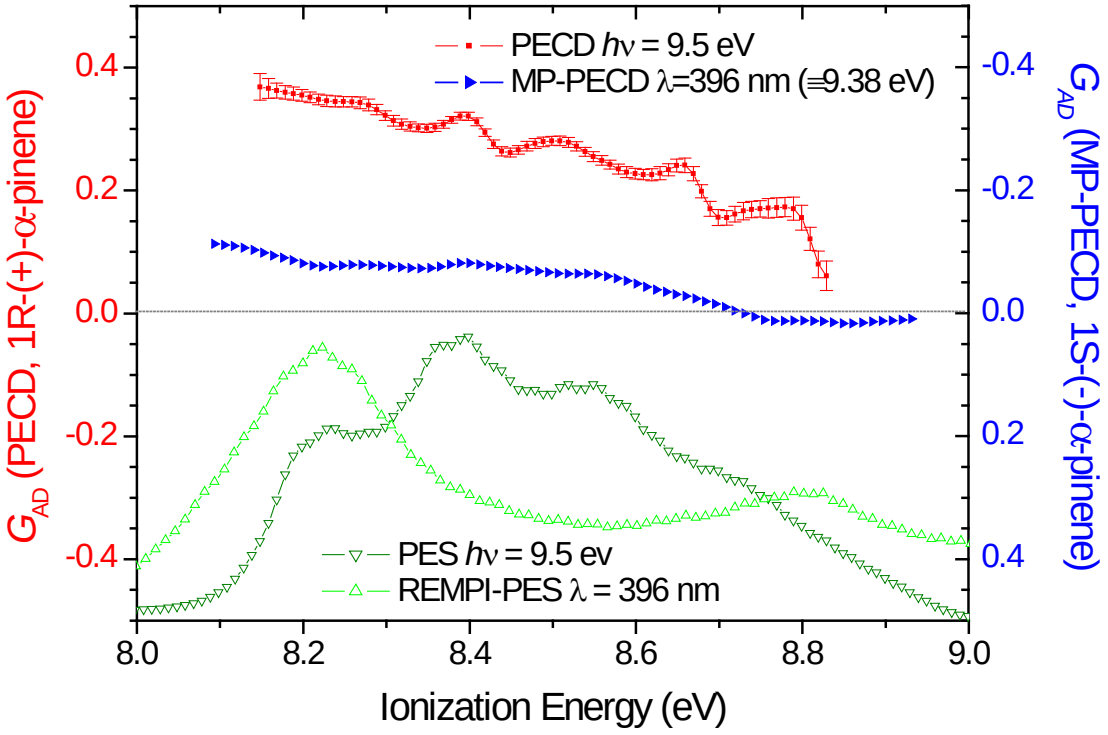

Figure 10

A comparison of the one-photon VUV PECD asymmetry factor $G_{AD}\ (=2b_1^{\{+1\}})$ recorded for R-(+)-α-pinene at a photon energy of 9.5 eV (taken from Ref. [34]), with the REMPI MP-PECD G_{AD} recorded for the S-(-) enantiomer at a laser wavelength 396 nm (equivalent three-photon energy 9.38 eV). As these experiments used different enantiomers, to simplify visual comparisons the plots are adjusted for the anticipated reversal of the asymmetry by inverting the MP-PECD plot axis direction. Also included are the corresponding PES (arbitrarily scaled) recorded in these different experiments, but having closely similar total energies.

References

[1]Ivan Powis, in *Adv. Chem. Phys.*, edited by J.C. Light (Wiley, New York, 2008), Vol. 138, Chap. 5 pp. 267-329.

[2]S. Turchini, *Journal of Physics: Condensed Matter* **29** (50), 503001 (2017); Laurent Nahon, Gustavo A. Garcia, and Ivan Powis, *J. Elec. Spec. Rel. Phen.* **204** (B), 322 (2015).

[3]Maurice H.M. Janssen and Ivan Powis, *Phys. Chem. Chem. Phys.* **16** (3), 856 (2014).

[4]B J Whitaker, *Imaging in Molecular Dynamics* (Cambridge University Press, Cambridge, 2003), p. 266.

[5]A. Bodi, P. Hemberger, T. Gerber, and B. Sztaray, *The Review of scientific instruments* **83** (8), 083105 (2012); X. F. Tang, G. A. Garcia, J. F. Gil, and L. Nahon, *Rev. Sci. Inst.* **86** (12), 123108 (2015).

[6]A. Vredenborg, W. G. Roeterdink, and M. H. M. Janssen, *Rev. Sci. Inst.* **79** (6), 063108 (2008).

[7]Ivan Powis, Steven Daly, Maurice Tia, Barbara Cunha de Miranda, Gustavo A. Garcia, and Laurent Nahon, *Phys. Chem. Chem. Phys.* **16** (2), 467 (2014); S. Daly, I. Powis, G.A. Garcia, H. Soldi-Lose, and L. Nahon, *J. Chem. Phys.* **134** (6), 064306 (2011); Laurent Nahon, Gustavo A. Garcia, Heloise Soldi-Lose, Steven Daly, and Ivan Powis, *Phys. Rev. A* **82** (3), art. no. 032514 (2010).

[8]Mohammad M. Rafiee Fanood, N. Bhargava Ram, C. Stefan Lehmann, Ivan Powis, and Maurice H.M. Janssen, *Nat. Commun.* **6**, 7511 (2015).

[9]K. L. Reid, *Ann. Rev. Phys. Chem.* **54**, 397 (2003); S. N. Dixit and V. McKoy, *J. Chem. Phys.* **82**, 3546 (1985); R. L. Dubs, V. McKoy, and S. N. Dixit, *J. Chem. Phys.* **88** (2), 968 (1988).

[10]C. N. Yang, *Phys. Rev.* **74** (7), 764 (1948).

[11]B. Ritchie, *Phys. Rev. A* **13**, 1411 (1976).

[12]Werner Kuhn and E. Braun, *Zeitschrift fur Physikalische Chemie* **8** (Abt. B), 445 (1930).

[13]Mohammad M. Rafiee Fanood, Maurice H. M. Janssen, and Ivan Powis, *J. Chem. Phys.* **145** (12), 124320 (2016).

[14]C. Stefan Lehmann, N. Bhargava Ram, Ivan Powis, and Maurice H.M. Janssen, *J. Chem. Phys.* **139** (23), 234307 (2013).

[15]C. Lux, M. Wollenhaupt, T. Bolze, Q. Q. Liang, J. Kohler, C. Sarpe, and T. Baumert, *Angew. Chem.-Int. Edit.* **51** (20), 5001 (2012).

[16]Christian Lux, Matthias Wollenhaupt, Cristian Sarpe, and Thomas Baumert, *ChemPhysChem* **16** (1), 115 (2015).

[17]A. Kastner, T. Ring, B. C. Kruger, G. B. Park, T. Schafer, A. Senftleben, and T. Baumert, *J. Chem. Phys.* **147** (1), 013926 (2017).

[18]Alexander Kastner, Greta Koumarianou, Pavle Glodic, Peter C. Samartzis, Nicolas Ladda, Simon T. Ranecky, Tom Ring, Sudheendran Vasudevan, Constantin Witte, Hendrike Braun, Han-Gyeol Lee, Arne Senftleben, Robert Berger, G. Barratt Park, Tim Schäfer, and Thomas Baumert, *Phys. Chem. Chem. Phys.* **22** (14), 7404 (2020).

[19]A. Comby, S. Beaulieu, M. Boggio-Pasqua, D. Descamps, F. Legare, L. Nahon, S. Petit, B. Pons, B. Fabre, Y. Mairesse, and V. Blanchett, *J. Phys. Chem. Lett.* **7** (22), 4514 (2016).

[20]A. Comby, E. Bloch, C. M. M. Bond, D. Descamps, J. Miles, S. Petit, S. Rozen, J. B. Greenwood, V. Blanchet, and Y. Mairesse, *Nat. Commun.* **9**, 5212, 5212 (2018).

[21]S. Beaulieu, A. Ferre, R. Geneaux, R. Canonge, D. Descamps, B. Fabre, N. Fedorov, F. Legare, S. Petit, T. Ruchon, V. Blanchet, Y. Mairesse, and B. Pons, *New J. Phys.* **18**, 102002 (2016).

[22]Mohammad M. Rafiee Fanood, Maurice H. M. Janssen, and Ivan Powis, *Phys. Chem. Chem. Phys.* **17**, 8614 (2015); S. Beaulieu, A. Comby, D. Descamps, S. Petit, F. Legare, B. Fabre, V. Blanchet, and Y. Mairesse, *J. Chem. Phys.* **149** (13), 134301 (2018).

[23]Mohammad M. Rafiee Fanood, Ivan Powis, and Maurice H. M. Janssen, *J. Phys. Chem. A* **118** (49), 11541 (2014).
[24]B. Schaefer, E. Collett, R. Smyth, D. Barrett, and B. Fraher, *Am. J. Phys.* **75** (2), 163 (2007).
[25]A. T. J. B. Eppink and D. H. Parker, *Rev. Sci. Inst.* **68** (9), 3477 (1997).
[26]D. Irimia, D. Dobrikov, R. Kortekaas, H. Voet, D. A. van den Ende, W. A. Groen, and M. H. M. Janssen, *Rev. Sci. Inst.* **80** (11), 113303 (2009).
[27]G. A. Garcia, L. Nahon, and I. Powis, *Rev. Sci. Inst.* **75** (11), 4989 (2004).
[28]M. J. Frisch, G. W. Trucks, H. B. Schlegel, G. E. Scuseria, M. A. Robb, J. R. Cheeseman, G. Scalmani, V. Barone, G. A. Petersson, H. Nakatsuji, X. Li, M. Caricato, A. V. Marenich, J. Bloino, B. G. Janesko, R. Gomperts, B. Mennucci, H. P. Hratchian, J. V. Ortiz, A. F. Izmaylov, J. L. Sonnenberg, D. Williams-Young, F. Ding, F. Lipparini, F. Egidi, J. Goings, B. Peng, A. Petrone, T. Henderson, D. Ranasinghe, V. G. Zakrzewski, J. Gao, N. Rega, G. Zheng, W. Liang, M. Hada, M. Ehara, K. Toyota, R. Fukuda, J. Hasegawa, M. Ishida, T. Nakajima, Y. Honda, O. Kitao, H. Nakai, T. Vreven, K. Throssell, Jr. J. A. Montgomery, J. E. Peralta, F. Ogliaro, M. Bearpark, J. J. Heyd, E. Brothers, K. N. Kudin, V. N. Staroverov, T. A. Keith, R. Kobayashi, J. Normand, K. Raghavachari, A. Rendell, J. C. Burant, S. S. Iyengar, J. Tomasi, M. Cossi, J. M. Millam, M. Klene, C. Adamo, R. Cammi, J. W. Ochterski, R. L. Martin, K. Morokuma, O. Farkas, J. B. Foresman, and D. J. Fox, Gaussian 16 Revision A.03 (Gaussian Inc., Wallingford, CT, 2016).
[29]Kestutis Aidas, Celestino Angeli, Keld L. Bak, Vebjørn Bakken, Radovan Bast, Linus Boman, Ove Christiansen, Renzo Cimiraglia, Sonia Coriani, Pål Dahle, Erik K. Dalskov, Ulf Ekström, Thomas Enevoldsen, Janus J. Eriksen, Patrick Ettenhuber, Berta Fernández, Lara Ferrighi, Heike Fliegl, Luca Frediani, Kasper Hald, Asger Halkier, Christof Hättig, Hanne Heiberg, Trygve Helgaker, Alf Christian Hennum, Hinne Hettema, Eirik Hjertenæs, Stinne Høst, Ida-Marie Høyvik, Maria Francesca Iozzi, Branislav Jansík, Hans Jørgen Aa. Jensen, Dan Jonsson, Poul Jørgensen, Joanna Kauczor, Sheela Kirpekar, Thomas Kjærgaard, Wim Klopper, Stefan Knecht, Rika Kobayashi, Henrik Koch, Jacob Kongsted, Andreas Krapp, Kasper Kristensen, Andrea Ligabue, Ola B. Lutnæs, Juan I. Melo, Kurt V. Mikkelsen, Rolf H. Myhre, Christian Neiss, Christian B. Nielsen, Patrick Norman, Jeppe Olsen, Jógvan Magnus H. Olsen, Anders Osted, Martin J. Packer, Filip Pawlowski, Thomas B. Pedersen, Patricio F. Provasi, Simen Reine, Zilvinas Rinkevicius, Torgeir A. Ruden, Kenneth Ruud, Vladimir V. Rybkin, Pawel Sałek, Claire C. M. Samson, Alfredo Sánchez de Merás, Trond Saue, Stephan P. A. Sauer, Bernd Schimmelpfennig, Kristian Sneskov, Arnfinn H. Steindal, Kristian O. Sylvester-Hvid, Peter R. Taylor, Andrew M. Teale, Erik I. Tellgren, David P. Tew, Andreas J. Thorvaldsen, Lea Thøgersen, Olav Vahtras, Mark A. Watson, David J. D. Wilson, Marcin Ziolkowski, and Hans Ågren, *WIREs Computational Molecular Science* **4** (3), 269 (2014).
[30]Takeshi Yanai, David P. Tew, and Nicholas C. Handy, *Chem. Phys. Lett.* **393** (1), 51 (2004).
[31]K. Kaufmann, W. Baumeister, and M. Jungen, *J. Phys. B-At. Mol. Opt. Phys.* **22** (14), 2223 (1989).
[32]C. L. Qiu, J. Smuts, and K. A. Schug, *Journal of Separation Science* **40** (4), 869 (2017).
[33]Dhirendra P. Singh, PhD, University of Nottingham, 2020.
[34]Hassan Ganjitabar, Rim Hadidi, Gustavo Garcia, Laurent Nahon, and Ivan Powis, *J. Mol. Spec.* **353**, 11 (2018).
[35]Hassan Ganjitabar, Gustavo Garcia, Laurent Nahon, and Ivan Powis, *J. Chem. Phys.* **153** (3), 034302 (2020).
[36]D. Kubala, E. A. Drage, A. M. E. Al-Faydhi, J. Kocisek, P. Papp, V. Matejcik, P. Mach, J. Urban, P. Limao-Vieira, S. V. Hoffmann, S. Matejcik, and N. J. Mason, *Int. J. Mass. Spec.* **280** (1-3), 169 (2009).
[37]R. E. Goetz, T. A. Isaev, B. Nikoobakht, R. Berger, and C. P. Koch, *J. Chem. Phys.* **146** (2), 024306 (2017).
[38]J. Miles, D. Fernandes, A. Young, C. M. M. Bond, S. W. Crane, O. Ghafur, D. Townsend, J. Sá, and J. B. Greenwood, *Analytica Chimica Acta* **984**, 134 (2017).

[39]Samuel Beaulieu, Antoine Comby, Baptiste Fabre, Dominique Descamps, Amélie Ferré, Gustavo Garcia, Romain Géneaux, Francois Légaré, Laurent Nahon, Stéphane Petit, Thierry Ruchon, Bernard Pons, Valérie Blanchet, and Yann Mairesse, *Faraday Discuss.* **194**, 325 (2016).